

EXPERIMENTAL RF BREAKDOWN STUDY BASED ON DIRECT IN-SITU OBSERVATION OF NORMAL-CONDUCTING ACCELERATING CAVITIES

Tetsuo Abe*, Tatsuya Kageyama, Hiroshi Sakai, Yasunao Takeuchi, and Kazuo Yoshino
High Energy Accelerator Research Organization (KEK), Tsukuba, Japan

Abstract

In our previous study on a normal-conducting 508.9-MHz continuous-wave accelerating cavity, it was discovered that most breakdown events were accompanied by the explosion of a stable bright spot on one of the two end plates of the cavity (Breakdown Type I) or by a spot-type explosion not originating from a stable bright spot (Breakdown Type II); both of these explosions can be understood as breakdown triggers. In the present study, the light emitters of stable bright spots in Breakdown Type I and the dynamics of spot-type explosions in Breakdown Type II were investigated using hyperspectral and high-speed cameras, respectively.

INTRODUCTION

Normal-conducting radio-frequency (rf) accelerating cavities (hereafter simply “cavities”), composed of oxygen-free copper, are at the hearts of many modern particle accelerators. A vacuum arc in a cavity can lead to cavity breakdown, which can limit the accelerator performance; however, the actual trigger mechanism of cavity breakdowns is unknown despite many breakdown studies having been performed by many researchers around the world (e.g., presentations from recent workshops [1, 2]).

In 2014, we performed an experimental breakdown study on a normal-conducting 508.9-MHz continuous-wave accelerating cavity based on direct in-situ observation [3] guided by the conviction that a “direct” picture is worth a thousand “indirect” measurements. This conviction has been inspired by an assumption that a trigger of cavity breakdown (breakdown trigger) is so tiny that its information can be mostly destroyed by a huge phenomenon of cavity breakdown. In this previous study, the inside of the cavity was directly observed using three television (TV) cameras during a high-power test, and videos were recorded at the moment of cavity breakdowns. From these observations, it was discovered that breakdown events of interest could be classified into two types. The first type is accompanied by an explosion of a stable bright spot on one of the two end plates of the cavity; prior to explosion, this bright spot was observed to maintain its intensity for hours or longer with no significant effects on the accelerating mode field during high-power operation (Breakdown Type I). No observed breakdown events were accompanied by two or more explosions of stable bright spots; therefore, such an explosion must be a breakdown trigger. Another

type was accompanied by a spot-type (i.e., localized) explosion not originating from a stable bright spot (Breakdown Type II). As before, no observed breakdown event was accompanied by two or more such explosions, which means that such explosions also must be breakdown triggers. Breakdown Types I and II constituted approximately 25% and 40% of the 205 total breakdown events. The remaining events (approximately 35%) consisted of “pyrotechnical” breakdown events accompanied by a non-spot-type flash or non-spot-type lightning (approximately 10%) and breakdown events accompanied by no abnormality observed by any of the three TV cameras at the moment of cavity breakdown (approximately 25%). Because breakdown events accompanied by a non-spot-type flash or non-spot-type lightning were observed only in the initial stage of rf conditioning, essential points of investigation required to elucidate the breakdown trigger mechanism in normal-conducting ultrahigh-frequency continuous-wave cavities are (1) the light emitters of stable bright spots in Breakdown Type I and (2) the dynamics of spot-type explosions in Breakdown Type II.

A complete version of this paper is available from [4].

RF ACCELERATING CAVITIES

For a positron damping ring (DR) at the SuperKEKB accelerator [5], we previously developed normal-conducting 508.9-MHz accelerating cavities made of high-purity oxygen-free copper (C10100, ASTM F68 Class 1) with a complete higher-order-mode (HOM) heavily damped structure; this type of cavity is hereafter referred to as the DR cavity [6–9]. We fabricated a prototype cavity (DR cavity No. 0) in fiscal year 2011 and performed the first high-power test of this cavity early in fiscal year 2012 at a high-power test stand. Then, based on the development results of DR cavity No. 0, we fabricated two production versions of the DR cavity, the first (DR cavity No. 1) in fiscal year 2012 and the second (DR cavity No. 2) in fiscal year 2013. Details on the DR cavities are given in [3, 5–9].

Whereas DR cavity No. 2 was used in our previous study [3], DR cavity No. 0 was used in this study. DR cavity No. 0 was successfully conditioned up to an accelerating voltage per cavity (cavity voltage V_c) of 0.90 MV and an equivalent accelerating gradient E_{acc} of 3.5 MV/m, that is radiation limit of the test stand, and it showed a high-power performance comparable to those of DR cavities No. 1 and No. 2. The present study was performed during the second high-power test of DR cavity No. 0 in 2017.

* tetsuo.abe@kek.jp

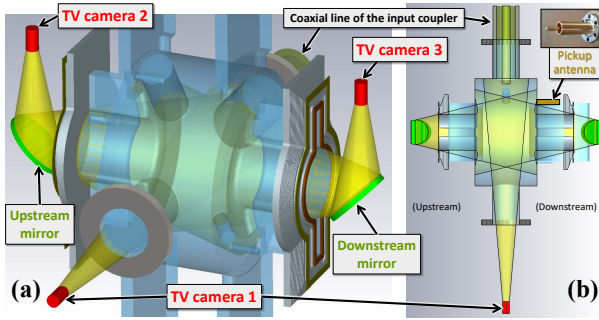


Figure 1: (a) Schematic of the experimental setup for multidirectional and wide-field observation. The red cylinders and yellow regions represent the three TV cameras and their fields of view, respectively. During the high-power test, the inside of the cavity (blue) was a vacuum, and the mirrors (green) were contained in the mirror chambers. (b) Cross-sectional view of the experimental setup along the horizontal plane including the center of the cavity.

EXPERIMENTAL SETUP

Because the experimental setup is the same as that in our previous study [3] except for the cameras, only an overview is presented in this section.

High rf power was fed into the cavity through a coaxial-type high-power input coupler with a coupling loop at the end of the coaxial line. On each of the upstream and downstream beam ports, a vacuum chamber containing an elliptical mirror (mirror chamber) was mounted to allow the direct in-situ observation of the inside of the cavity through the beam port. Three TV cameras were positioned as shown in Fig. 1 for multidirectional and wide-field observation, where TV camera 1 was always a high-speed camera, and either both TV cameras 2 and 3 were high-speed cameras or one was a hyperspectral camera.

SPECTRA OF STABLE BRIGHT SPOTS

Hyperspectral Camera

To investigate the light emitters of stable bright spots in Breakdown Type I, their spectra were measured using a hyperspectral camera (NH-3, EBA JAPAN Co., Ltd. [10]). This camera is based on line scanning for one-dimensional spectroscopy, and moving the line-scanning system mechanically enables two-dimensional (2D) spectroscopy.

Pixel Sensitivity Calibration

The pixel sensitivity calibration was initially performed in 2015 before the delivery of the hyperspectral camera, and a second calibration was performed in 2017 with the same setup as in 2015 after all of the spectrum measurements in this study; the reference spectrum was found to have changed between these two calibrations, as shown in Fig. 2b. The reason for this difference has not yet been conclusively determined; however, a possible cause is the occurrence of radiation damage during the high-power test in

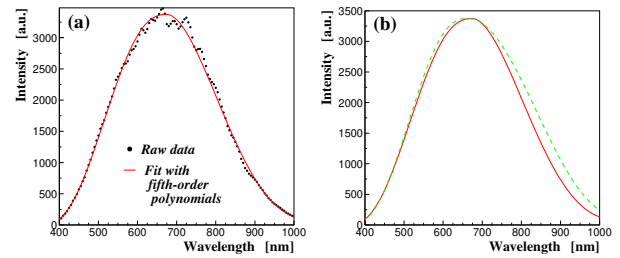


Figure 2: Spectrum measurements for the uniform light emitted by the integrating sphere. (a) Observed raw data (black dots) taken in 2015 before the delivery of the hyperspectral camera. (b) Reference spectrum from the data taken in 2015 (red curve, same as the reference spectrum in (a)) and the reference spectrum from the data taken in 2018 after all of the spectrum measurements in this study (dashed green curve).

the test stand. This difference will be included as a systematic error in the final results presented later in this paper.

Wavelength Calibration

The absolute wavelength was calibrated using a red HeNe laser, which has a single wavelength of 632.8 nm.

Correction Factor to Convert Observed Spectra to Physical Spectra

Even if the pixel sensitivity calibration is applied, the wavelength-dependent efficiency of the hyperspectral camera cannot be corrected; that is, the observed spectra cannot be converted to physical spectra unless the true spectrum of the light source used in the pixel sensitivity calibration is known. To obtain a correction factor for this conversion, thermal radiation spectra from a high-temperature cylinder made of copper (copper cylinder) were used, and the temperature of the copper cylinder was measured with type-K thermocouples. To heat the copper cylinder, an electron-beam welding (EBW) machine was used.

Planck's law is given by

$$\mathcal{E} \propto \frac{1}{\lambda^5} \frac{1}{e^{\frac{hc}{\lambda kT}} - 1}, \quad (1)$$

where \mathcal{E} is the energy density, λ is the wavelength, T is the temperature, c is the speed of light, k is the Boltzmann constant, and h is the Planck constant. Figure 3 shows the correction factor as a function of the wavelength; in each plot, there are eight black curves corresponding to the four temperature points at each of the two considered thermocouples (TC4 and TC5). The eight black curves are very close to each other, which means that black-body radiation was correctly measured from TC4 and TC5. The average among the eight black curves in Fig. 3 (red curve) was used to derive the physical spectra, as described in the following section.

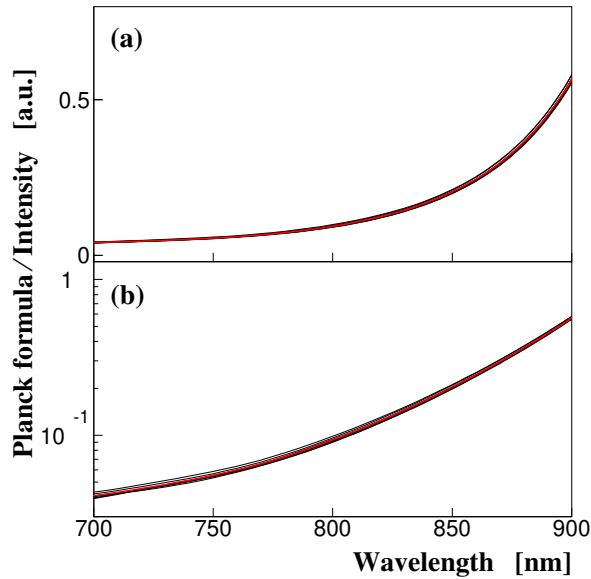


Figure 3: Correction factor to convert observed spectra to physical spectra as a function of the wavelength on (a) linear and (b) logarithmic scales. The red curve is the average of the eight black curves.

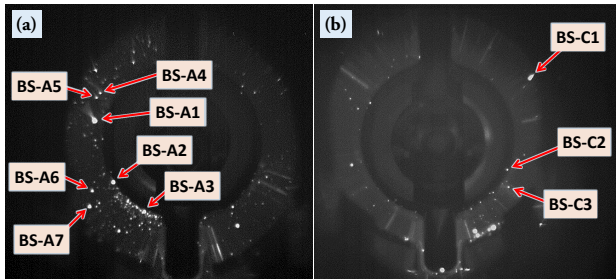


Figure 4: Snapshots of the (a) upstream and (b) downstream end plates during the high-power test of DR cavity No. 0 at $V_c = 0.80$ MV, taken by the high-speed camera. The labels give the names of the bright spots used for reference in this paper.

Measurement Results

The spectra of the 10 stable bright spots shown in Fig. 4 were measured by integrating the spectra around each bright spot to avoid the defocus effect. Correction was applied for the reflectance of the mirror and the transmissivity of the viewing port window of the mirror chamber (mirror chamber correction) in a manner similar to that used to estimate the transmissivity of the viewing window of the EBW machine, although the correction had only a small effect. Figure 5 shows the observed spectra of BS-A1 and BS-A2, which were respectively the brightest and second brightest spots on the upstream end plate, together with that of BS-C1, which was the brightest spot on the downstream end plate. As shown in this figure, there is no line or band spectrum in the visible light and near-infrared regions, and the spectra move toward lower wavelengths at higher cavity voltages. In the same way, no significant line or band

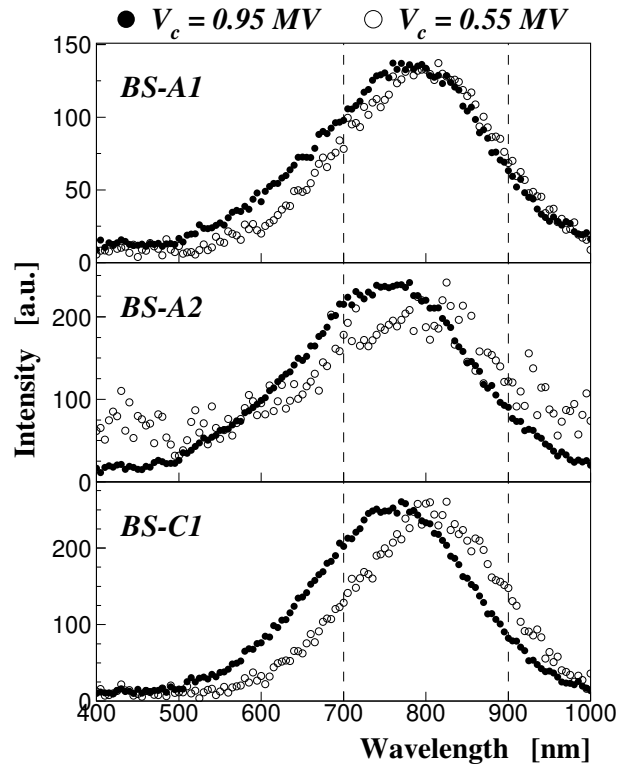


Figure 5: Observed spectra of the stable bright spots BS-A1, BS-A2, and BS-C1 after applying the pixel sensitivity and wavelength calibrations, the mirror-chamber correction, and background subtraction. The vertical dashed lines indicate the region in which the physical spectra were derived.

spectra were observed for the other bright spots. This observation means that these bright spots are caused by thermal radiation.

The next step was to measure the temperatures of the light emitters of the stable bright spots. Applying the correction factor shown in Fig. 3 to the observed spectra yielded the physical spectra; an example of such a physical spectrum is shown in Fig. 6. The spectra were fitted with Planck's law, and the temperature was obtained from this fitting, as shown in Fig. 6. The wavelength range was divided into two regions, 700 to 800 nm and 800 to 900 nm, to address the possibility of a nonuniform temperature distribution. The error of the temperature was calculated such that the χ^2 value in the fitting divided by the number of degrees of freedom is unity. Table 1 shows a list of temperatures obtained using this method for all the 10 stable bright spots, where the temperatures were calculated twice based on the two reference spectra shown in Fig. 2b because the reference spectrum in the pixel sensitivity calibration was different. The true value of temperature is expected to be between these two estimates.

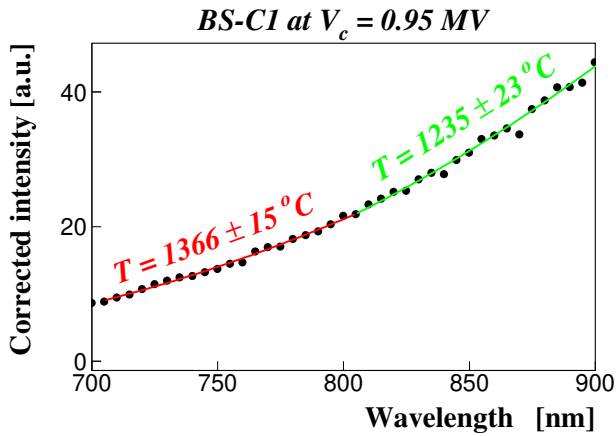


Figure 6: Example of a physical spectrum (corrected spectrum) obtained for BS-C1. The red and green curves are results of fitting the data with Planck's law in the wavelength regions of 700–800 nm and 800–900 nm, respectively. The temperatures obtained from these fitting results are also given.

Table 1: Measured temperatures in degrees Celsius of the light emitters of the stable bright spots for the wavelength regions of 700 to 800 nm and 800 to 900 nm based on the reference spectrum in the pixel sensitivity calibration performed in 2015 (solid red curve in Fig. 2b). Numbers enclosed in square brackets are temperatures calculated on the assumption that the reference spectrum changed to the dashed green curve shown in Fig. 2b before the spectrum measurement of the stable bright spots was initiated.

Name of bright spot	$V_c = 0.55$ MV		$V_c = 0.95$ MV	
	700 to 800 nm	800 to 900 nm	700 to 800 nm	800 to 900 nm
BS-A1	1072 ± 20 [1209 ± 22]	904 ± 19 [1124 ± 27]	1207 ± 13 [1369 ± 14]	1005 ± 19 [1266 ± 26]
BS-A2	1253 ± 58 [1428 ± 72]	865 ± 68 [1080 ± 98]	1440 ± 20 [1653 ± 17]	1178 ± 31 [1548 ± 40]
BS-A3	N/A	N/A	1057 ± 22 [1192 ± 25]	1095 ± 27 [1394 ± 41]
BS-A4	N/A	N/A	1028 ± 23 [1146 ± 26]	891 ± 47 [1109 ± 66]
BS-A5	N/A	N/A	1316 ± 38 [1494 ± 48]	979 ± 42 [1218 ± 64]
BS-A6	N/A	N/A	1349 ± 37 [1560 ± 46]	859 ± 34 [1086 ± 51]
BS-A7	N/A	N/A	1155 ± 45 [1340 ± 57]	833 ± 36 [1052 ± 53]
BS-C1	933 ± 26 [1022 ± 31]	844 ± 22 [1008 ± 26]	1366 ± 15 [1535 ± 14]	1235 ± 23 [1546 ± 29]
BS-C2	N/A	N/A	1182 ± 43 [1325 ± 49]	1158 ± 65 [1502 ± 95]
BS-C3	N/A	N/A	1250 ± 33 [1418 ± 44]	1088 ± 71 [1396 ± 101]

OBSERVATION OF FLYING BRIGHT OBJECTS

To investigate the dynamics of spot-type explosions in Breakdown Type II, direct in-situ observation was performed using three high-speed cameras (HAS-D3M, DI-TECT Co., Ltd. [11]), these cameras can be synchronized frame by frame. The maximum frame rate is 100,000 frames per second (fps); however, frame rates of only 1,000

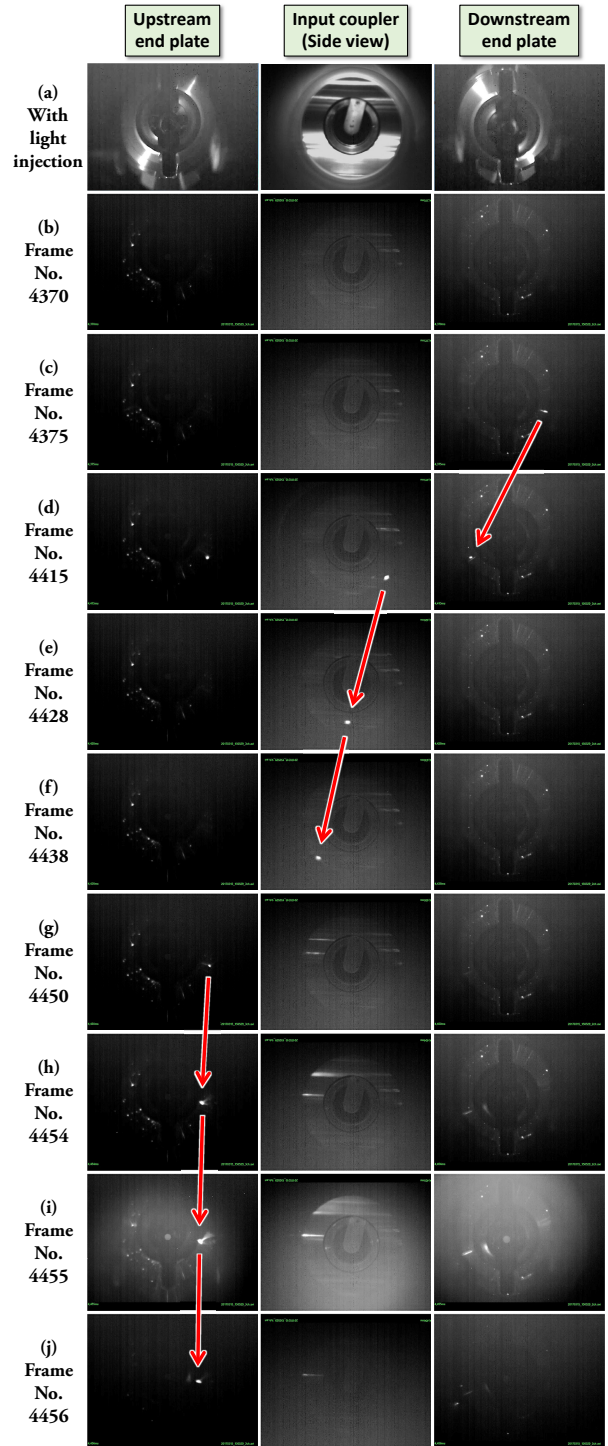


Figure 7: First breakdown event accompanied by a flying bright object, which occurred at $V_c = 0.88$ MV, 15:05 on March 15 in 2017. (a) Photographs showing the view of the high-speed cameras with light injected into the cavity for visualization. (b)–(j) Snapshots synchronized among the three high-speed cameras recorded at 1,000 fps. Red arrows indicate the flying bright object of interest. The brightness of all images was enhanced by 60% relative to the original brightness.

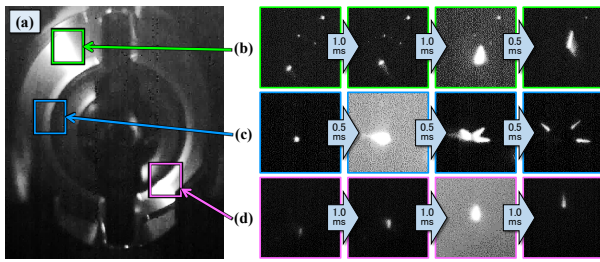


Figure 8: Three other breakdown events accompanied by a flying bright object. The brightness and contrast of the all the images were enhanced by 60% and 40% relative to the original brightness and contrast, respectively. (a) Photograph showing the view of the high-speed camera directed toward the downstream end plate with light injected into the cavity for visualization. Snapshots of the (b) second, (c) third, and (d) fourth breakdown events around the time of cavity breakdown. These are magnified views of the regions shown with (b) green, (c) blue, and (d) magenta squares in (a).

or 2,000 fps were used in this study because the intensity in each frame was too low at frame rates above 2,000 fps.

Videos obtained using the high-speed cameras were automatically saved to a computer storage device during the time period from a few seconds before the rf switch of the low-level control system was changed from ON to OFF, which is the recording trigger signal, until approximately 10 ms after this change.

With the setup using the three high-speed cameras as TV cameras No. 1, No. 2, and No. 3 in Fig. 1, 40 breakdown events were detected. In four of these events, a flying bright object was observed to impact the end-plate surface at the moment of cavity breakdown. Figure 7 shows one of these four events, where the gravitational force is directed vertically downward in each snapshot. Nothing was observed until frame No. 4370 (Fig. 7b). A bright spot appeared at 4 o'clock on the downstream end plate after frame No. 4370; it then moved toward the upstream end plate and impacted the surface of the end plate in frame No. 4455. In the next frame (No. 4456), the intensities of the stable bright spots dropped; therefore, cavity breakdown occurred at the moment of impact observed in frame No. 4455, which means that the impact triggered the cavity breakdown. In three other breakdown events of the same type, a flying bright object impacted the surface of the downstream end plate at the moment of cavity breakdown, as shown in Fig. 8. The event shown in Fig. 8c can be understood as a flying object perpendicularly impacting the end-plate surface and breaking into three pieces.

CONCLUSIONS

Using the hyperspectral camera, we made the first measurement of the spectra and temperatures of stable bright

spots, which are known to be a potential trigger of cavity breakdown, and discovered that the light emitters of stable bright spots are not copper but contamination microparticles with a high melting or sublimation point (higher than 1000 °C at a pressure of 2×10^{-5} Pa). In addition, using the high-speed cameras, we made the novel observation of breakdown events accompanied by a flying bright object impacting an end-plate surface, triggering cavity breakdown.

On the basis of the observations in this study, we formed the following hypotheses: (1) Breakdown Type I can be understood as a physical process in which a microparticle with a temperature exceeding 1000 °C interacts with other materials at the same position, leading to an explosion and triggering cavity breakdown; and (2) Breakdown Type II can be understood as a physical process in which a high-temperature charged microparticle accelerates and impacts an end-plate surface, leading to an explosion on the surface and triggering cavity breakdown.

REFERENCES

- [1] "7th International Workshop on Mechanisms of Vacuum Arcs (MeVArc2018)." MeVArc2018; <https://indico.cern.ch/event/680402/>
- [2] "11th International Workshop on Breakdown Science and High Gradient Technology (HG2018)." HG2018; <https://indico.cern.ch/event/675785/>
- [3] T. Abe, T. Kageyama, H. Sakai, Y. Takeuchi, and K. Yoshino, "Breakdown study based on direct in situ observation of inner surfaces of an rf accelerating cavity during a high-gradient test," *Phys. Rev. Accel. Beams*, vol. 19, no. 10, p. 102001, 2016; <https://journals.aps.org/prab/abstract/10.1103/PhysRevAccelBeams.19.102001>.
- [4] <https://lib-extopc.kek.jp/preprints/PDF/2018/1827/1827026.pdf>
- [5] "SuperKEKB Design Report"; <http://www-superkekb.kek.jp/documents.html>
- [6] T. Abe, T. Kageyama, Y. Takeuchi, H. Sakai, and K. Yoshino, in *Proceedings of the 8th Annual Meeting of Particle Accelerator Society of Japan, TUPS131*, August 2011.
- [7] T. Abe, Y. Takeuchi, T. Kageyama, H. Sakai, and K. Yoshino, in *Proceedings of the 9th Annual Meeting of Particle Accelerator Society of Japan, THLR06*, August 2012.
- [8] T. Abe, Y. Takeuchi, T. Kageyama, H. Sakai, and K. Yoshino, in *Proceedings of the 10th Annual Meeting of Particle Accelerator Society of Japan, SAP057*, August 2013.
- [9] T. Abe, Y. Takeuchi, T. Kageyama, H. Sakai, and K. Yoshino, in *Proceedings of the 11th Annual Meeting of Particle Accelerator Society of Japan, SAP050*, August 2014.
- [10] <https://ebajapan.jp/English/>
- [11] <http://www.ditect.co.jp/en/>